AGU PUBLICATIONS

JGR

Journal of Geophysical Research: Atmospheres

RESEARCH ARTICLE

10.1002/2017JD027718

Key Points:

- A new analysis of NEXRAD radar data shows the spatial and temporal occurrence of tropopause-overshooting convection over the United States
- Ten years of high-resolution gridded NEXRAD data (GridRad) are now available through the NCAR Research Data Archive
- Overshooting convection is most common over the central United States; almost half of observed overshooting events reach 380 K or higher

Correspondence to:
K. P. Bowman,
k-bowman@tamu.edu

Citation:
Cooney, J. W., Bowman, K. P., Homeyer, C. R., & Fenske, T. M. (2018). Ten year analysis of tropopause-overshooting convection using GridRad data. *Journal of Geophysical Research: Atmospheres*, *123*, 329–343. https://doi.org/10.1002/2017JD027718

Received 8 SEP 2017
Accepted 21 DEC 2017
Accepted article online 3 JAN 2018
Published online 15 JAN 2018

Ten Year Analysis of Tropopause-Overshooting Convection Using GridRad Data

John W. Cooney[1], Kenneth P. Bowman[1], Cameron R. Homeyer[2], and Tyler M. Fenske[1]

[1]Department of Atmospheric Sciences, Texas A&M University, College Station, TX, USA, [2]School of Meteorology, University of Oklahoma, Norman, OK, USA

Abstract Convection that penetrates the tropopause (overshooting convection) rapidly transports air from the lower troposphere to the lower stratosphere, potentially mixing air between the two layers. This exchange of air can have a substantial impact on the composition, radiation, and chemistry of the upper troposphere and lower stratosphere (UTLS). In order to improve our understanding of the role convection plays in the transport of trace gases across the tropopause, this study presents a 10 year analysis of overshooting convection for the eastern two thirds of the contiguous United States for March through August of 2004 to 2013 based on radar observations. Echo top altitudes are estimated at hourly intervals using high-resolution, three-dimensional, gridded, radar reflectivity fields created by merging observations from available radars in the National Oceanic and Atmospheric Administration Next Generation Weather Radar (NEXRAD) network. Overshooting convection is identified by comparing echo top altitudes with tropopause altitudes derived from the ERA-Interim reanalysis. It is found that overshooting convection is most common in the central United States, with a weak secondary maximum along the southeast coast. The maximum number of overshooting events occur consistently between 2200 and 0200 UTC. Most overshooting events occur in May, June, and July when convection is deepest and the tropopause altitude is relatively low. Approximately 45% of the analyzed overshooting events (those with echo tops at least 1 km above the tropopause) have echo tops extending above the 380 K level into the stratospheric overworld.

1. Introduction and Background

Deep convective storms contain thermally driven updrafts that rapidly lift boundary layer and lower tropospheric air into the upper troposphere and lower stratosphere (UTLS). Deep convection occurs around the globe, but its juxtaposition with lower tropopause altitudes in the extratropics enables deep penetration into the lower stratosphere (Liu & Liu, 2016; Solomon et al., 2016; Wang, 2003), where mass exchange of trace constituents can have a significant impact on UTLS composition (Dessler & Sherwood, 2004). In the UTLS, trace gases have a major impact, both directly and indirectly, on chemistry, dynamics, and radiation (Gettelman et al., 2011; Holton et al., 1995; Stohl et al., 2003). Many radiatively and chemically important species have long lifetimes in the UTLS, so their distribution is predominantly determined by transport processes. Because the transport by the Brewer-Dobson circulation is downward in the extratropics, air injected a short distance into the stratosphere (below the 380 K potential temperature level and 1 to 2 km above the tropopause) will have a short residence time in the stratosphere. Air injected to higher altitudes, however, particularly into the stratospheric overworld (above the ~380 K level), will have a longer stratospheric residence time, can be transported long distances, and can have a larger impact on stratospheric processes (Stohl et al., 2003). Over North America, in particular, the quasi-stationary anticyclone that dominates the summer circulation may confine water vapor and other tropospheric constituents for extended periods. Determining how small-scale processes, including convection, contribute to transporting air across the tropopause is vital for understanding future changes in the composition and structure of the UTLS as well as how these changes will affect the stratosphere and Earth's climate (Anderson et al., 2012, 2017).

Model simulations have demonstrated that mass exchange across the tropopause by deep convection plays a significant role in the composition and chemistry of the UTLS (Chagnon & Gray, 2010; Gray, 2003; Homeyer et al., 2017; Wang, 2007). These studies typically focus on a single convective event or a small number of events that occur during a field campaign. Case studies can provide insight into the mechanisms of transport by deep convection, but they yield little information about the frequency and distribution of tropopause-penetrating convection, which is necessary for a full quantitative picture of stratosphere-troposphere exchange (STE).

Satellite data have also been used to assess the role deep convection plays in STE. For example, Berendes et al. (2008), Lindsey and Grasso (2008), and Rosenfeld et al. (2008) detect tropopause-penetrating convection through different techniques using visible or near-infrared texture and reflectance. These techniques perform well at certain times but suffer from enhanced texture at large solar zenith angles, limiting their coverage of the diurnal cycle. For instance, over the Great Plains and western Great Lakes region, Bedka et al. (2010) find that approximately 60%–75% of overshooting events occur at night and would therefore be missed by daytime-only algorithms.

Bedka et al. (2010) attempt to overcome these limitations by combining conventional meteorological analyses and satellite infrared (IR) brightness temperature spatial gradients in a 5 year climatology of overshooting convection in the United States. In that analysis, tropopause-overshooting convection is identified by comparing the analyzed tropopause temperature and the observed brightness temperature at each grid point in their domain. The algorithm requires overshooting features to be at least 6.5 K colder than the surrounding anvil temperatures. This technique is able to identify storms missed by daytime-only algorithms and works well in most cases, but has some limitations of its own. Depending on the magnitude of overshooting and the quality control settings implemented, the infrared window texture method has a false-alarm rate that ranges from 4.2% to 38.8% (Bedka et al., 2010), primarily because IR signatures are not necessarily unique. For example, the large-scale algorithms do not account for cooling of surrounding air by sublimation of ice particles within an updraft. This causes updrafts at levels near the tropopause to appear in the IR retrieval as cooler than the tropopause and incorrectly flags the event as an overshoot.

An alternative observational approach is to use ground-based meteorological radars to identify echoes above the tropopause. Multiple radars in the U.S. NEXRAD network can be merged into three-dimensional grids (typically longitude, latitude, and altitude) by using a variety of selection and averaging algorithms. This reduces storage requirements and makes the data easier to use (e.g., Zhang et al., 2005, 2011; Lakshmanan et al., 2006; Langston et al., 2007; Ruzanski & Chandrasekar, 2012). Homeyer (2014) and Homeyer and Kumjian (2015) show that information about the vertical extent of deep convection is preserved in gridded WSR-88D observations when there are overlapping observations from multiple radars. Gridded values that include data from three or more radars yield a threefold increase in the vertical resolution when compared to an individual radar (i.e., the usable Δz is reduced from $\sim$3 km on average to $<$1 km).

Following the approach of Homeyer (2014) and Homeyer and Kumjian (2015), Solomon et al. (2016) combined multiple radars in the NEXRAD network to study the occurrence of tropopause-penetrating convection at 3 h intervals for a single year (2004) over the eastern United States. Solomon et al. (2016) defines tropopause-overshooting convection as any event in which a radar measures at least a 10 dBZ echo above the altitude of the tropopause. That study found a distinct geographic pattern in the frequency of overshooting convective events as well as clear diurnal and annual cycles. A majority of the observed overshooting events occur over the high plains around 0000 UTC ($\sim$1800 LT). Events occur most frequently during the warm season, with May having the highest number of individual overshooting storms. Solomon et al. (2016) show that overshooting events are infrequent east of the Mississippi River, which differs from the results of Bedka et al. (2010), who find overshooting to be common across the southeastern United States. The analysis in Solomon et al. (2016) covers a single calendar year with 3 h temporal resolution, so it is not clear whether the differences between their analysis and the 5 year analysis in Bedka et al. (2010) are due to differences in the observing systems, analysis methods, and overshoot definitions or to differences in the analysis periods.

To improve our understanding of overshooting convection, this study expands upon the approach in Solomon et al. (2016) by analyzing 10 years of NEXRAD data at hourly intervals across the eastern two thirds of the continental United States. Because a large fraction of the deep convection occurs during the warm season, we restrict the analysis to March, April, May, June, July, and August (MAMJJA). Increasing the sampling frequency and the length of the analysis period allows this study to address many of the limitations of the Solomon et al. (2016) analysis using a much larger data set. We also use updated methods to process the NEXRAD radar data into a new data set referred to as GridRad. GridRad, described in section 3.1, implements new techniques that are less restrictive than those used in Solomon et al. (2016), yielding a higher number of overshooting events and an improved understanding of their characteristics. The goals of this work are to introduce the GridRad data set and provide a climatology of the characteristics of overshooting convection over most of the contiguous United States.

2. Data

2.1. NEXRAD Data

Radar data were obtained from the National Oceanic and Atmospheric Administration (NOAA) National Centers for Environmental Information (NCEI, formerly known as the National Climate Data Center) NEXRAD web service (http://www.ncdc.noaa.gov). For all years available, NEXRAD Doppler S-band (10 cm wavelength) radars measure the radar reflectivity factor at horizontal polarization Z_H, radial velocity V_R, and velocity spectrum width σ_V in a volume around the radar by azimuthally scanning a conical beam with an angular width of 0.95° at multiple elevation angles (Crum & Alberty, 1993). When convection is occurring in the vicinity of a NEXRAD radar, the radar completes a total volume scan in approximately 4.5 to 5 min (Crum & Alberty, 1993). Data files containing volume scans are classified as Level 2 data products.

Over the years NOAA has modified the NEXRAD Level 2 data files to handle changes in data processing and radar capabilities. Level 2 data files created prior to May 2008 are referred to as "legacy resolution." Legacy resolution files contain three primary variables (Z_H, V_R, and σ_V) stored with a resolution of 1° in azimuth and 1 km in range. Beginning in May 2008 NEXRAD products transitioned to "superresolution," which is characterized by an azimuthal resolution of 0.5° and a range resolution of 250 m for the lowest three to five elevations (generally scans at 1.5° elevation or lower). Higher elevations of the superresolution files have 1° azimuthal resolution and 250 m range resolution. Beginning in May 2011, the NEXRAD radars were upgraded to dual polarization. The upgrade process was completed for all NEXRAD radars in 2013. Volumes from the dual-polarization radars include additional variables that are not used in this study. Here we only use Z_H.

NEXRAD radars are capable of sensing Z_H values well below those found in regions producing measurable precipitation, especially at ranges close to the radar. The minimum detectable signal is −42 dBZ at 1 km. This radar sensitivity decreases with range to about 11 dBZ at the maximum detectable range for Z_H of 460 km (Crum & Alberty, 1993). At 300 km, which is the maximum range used in this study for the merging of multiple radars, the minimum detectable signal is ∼7.5 dBZ (Homeyer, 2014).

To maximize the overlap between nearby radars and produce the highest-quality gridded product, the domain is restricted in this study to the eastern two thirds of the continental United States, where radar coverage is most dense. The analysis domain is a rectangular region bounded on the west and east by 115°W and 69°W longitude, and on the south and north by 25°N and 49°N latitude (Figure 1). The total area of the study domain is $\sim 10.8 \times 10^6$ km^2.

2.2. ERA-Interim Reanalysis

To identify tropopause-penetrating convection, tropopause altitudes are calculated using the ERA-Interim (ERA-I) reanalysis, which is produced by the European Centre for Medium-Range Weather Forecasts (ECMWF) (Dee et al., 2011). ERA-I data are also used in this study to calculate the potential temperature at the echo tops. ERA-I output is available from 1979 to the present and was obtained from the National Center for Atmospheric Research (NCAR) Research Data Archive (RDA; http://rda.ucar.edu/datasets/ds627.0/). Analyses are available at 6-hourly synoptic times (00, 06, 12, and 18 UTC) on a global grid with a longitude-latitude resolution of $\sim 0.7° \times \sim 0.7°$ and 37 irregularly spaced pressure levels extending from 1,000 to 1 hPa. Because the ERA-I data are on a coarser grid than the NEXRAD data (see section 3.1), temperature (T) and geopotential height (Z) are linearly interpolated in space and time to the NEXRAD grid for analysis. The tropopause height, z_T, is then calculated for each ERA-I column by applying the World Meteorological Organization (WMO) lapse rate tropopause definition (World Meteorological Organization, 1957). This approach is equivalent to that used in Homeyer (2014) and Solomon et al. (2016), where ERA-I tropopause altitudes were shown to agree with high-resolution radiosonde observations within ∼500 m. We conducted a similar comparison of the ERA-I and radiosonde-calculated tropopauses and found consistent results (not shown). Because the tropopause heights come from a global model, they do not account for perturbations in the tropopause due to the convection itself, and thus the uncertainty in the heights is not fully known. Aircraft observations and convection-allowing model simulations have shown that tropopause altitudes can be increased up to 1.5 km within air masses impacted by convection (Homeyer, Pan, Barth, 2014; Homeyer, Pan, Dorsi, et al., 2014).

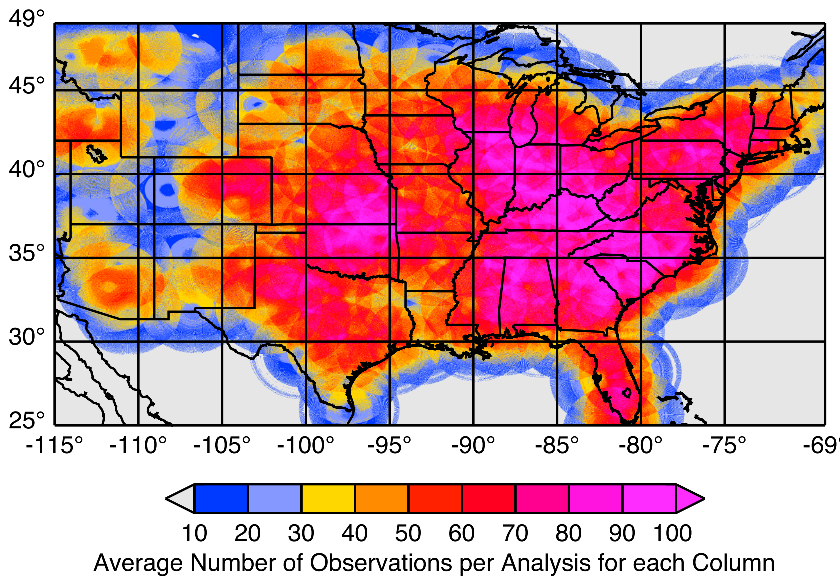

Figure 1. Average number of contributing NEXRAD radar observations per analysis time within each grid column during the March through August analysis period of 2004–2013. Locations with gray color fill are indicative of those with no or very few contributing NEXRAD radar observations and locations colored blue are indicative of inadequate radar coverage for reliable overshooting analysis.

3. Methods

3.1. NEXRAD Compositing

Data from individual NEXRAD radars are merged into hourly, high-resolution, three-dimensional, gridded, synoptic analyses using weighting in space and time. A summary of the gridding algorithm is provided here. Additional details can be found in the algorithm description document (Homeyer & Bowman, 2017). The current version of the gridding algorithm improves on the methods used in Solomon et al. (2016). The gridded NEXRAD WSR-88D radar data (Version 3.1), which are referred to as GridRad, are available for download from the RDA at NCAR (Bowman & Homeyer, 2017).

The analysis grid has a longitude-latitude resolution of 0.02° (∼2 km) and a vertical resolution of 1 km from 1 to 24 km above sea level. The value of a radar variable V on the GridRad grid is equal to the weighted average of all Level 2 observations in which echo is detected

$$V(x_i, y_j, z_k) = \frac{\sum_{n=1}^{N_{\mathrm{echo}}} w_n\, v_n}{\sum_{n=1}^{N_{\mathrm{echo}}} w_n}\,, \tag{1}$$

where N_{echo} is the number of Level 2 radar observations with echoes that contribute to the grid volume at location (x_i, y_j, z_k), and v_n and w_n are, respectively, the values of the observed radar variable and its weight for the nth Level 2 radar observation. The weights are given by

$$w(r,t) = e^{-r^2/L^2}\, e^{-\Delta t/\tau^2}\,, \tag{2}$$

where r is the radial distance of the radar observation from the radar location in km, Δt is the time difference between the observation and GridRad analysis time in seconds, $L = 150$ km is the spatial scale, and $\tau = 150$ s is the time scale. In the vertical, an individual radar beam is restricted to contribute only within a 1.5 km deep layer centered on the beam (up to three vertical grid boxes), which improves the representation of the internal structure and depth of storms in the merged data set compared to alternative approaches that allow deeper averaging depths. Hourly analyses (00, 01, …, 23 UTC) are created using all available NEXRAD volume scans within a ±3.8 min window centered on the analysis time. Echoes that have limited Level 2 observations and low weights are filtered from the gridded data prior to application of the echo top identification algorithm.

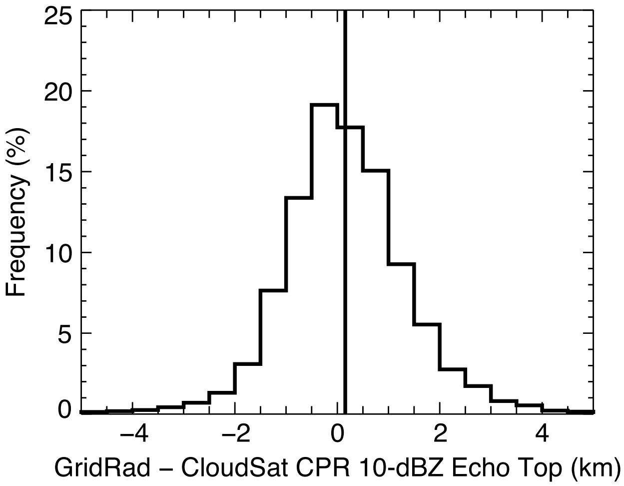

Figure 2. Frequency distribution of the difference in 10 dBZ echo top altitudes from GridRad and the CloudSat CPR over the contiguous United States during the period from 2006 to 2016. This comparison comprises 237,557 coincident radar reflectivity profiles.

The ability to detect overshooting convection in the GridRad data is constrained by the radar coverage. Figure 1 shows the average number of individual NEXRAD radar observations per analysis that contribute to each GridRad column during the 2004–2013 analysis period of this study. Blue colors indicate locations where the radar coverage is below that necessary for reliable convective overshooting identification. Most of these locations have poor sampling at altitudes greater than 12 km. Gaps occur in the mountain west, where radar coverage is limited by terrain and radar spacing, and around the edges of the network. Gaps are uncommon in the interior of the domain east of 100°W.

3.2. Echo Top Height Identification

The primary radar variable of interest in this study is the instantaneous, two-dimensional, gridded, echo top height, which is computed from each hourly, three-dimensional Z_H field. Before computing the echo top heights, however, the Z_H fields are subjected to three quality control processes. First, "echo holes" in the NEXRAD composites are found and filled. An echo hole is a gap in a vertical reflectivity profile that is no more than a single-level deep with valid measurements in the altitude bins immediately above and below that level. Echo holes are filled by averaging the Z_H values (in dBZ) for the two surrounding altitude bins (Homeyer & Kumjian, 2015). Second, the NEXRAD data are decluttered following an approach similar to that outlined in Zhang et al. (2004). This is done in order to remove the various types of nonmeteorological echoes that can arise in the 3-D regional NEXRAD composites. The decluttering algorithm assumes that precipitation and nonprecipitation echoes have different horizontal and vertical reflectivity structures when computed with respect to height (Zhang et al., 2004). The types of echoes are then identified from the features in the variations. Following decluttering, Z_H in grid boxes with low echo frequencies (the ratio of the number of contributing radar observations with echo to the total number of radar observations) is removed. The resulting quality-controlled Z_H fields are used for the echo top height analysis.

The echo top height, z_e, is defined in this study as the highest altitude in each column with a Z_H value that exceeds a specified threshold, with additional conditions aimed at isolating deep convection discussed below. Echo top heights are discretized into 1 km levels as a result of the GridRad vertical resolution. Due to the limited sensitivity of NEXRAD radars to small particles, the identified z_e is not, in general, the cloud top height. The nominal reflectivity threshold for the existence of a valid echo is ~5 dBZ. Lower-reflectivity thresholds might provide a better estimate of the cloud top height, but would also result in a higher incidence of errors and artifacts due to clutter and side lobe contamination. After extensive testing with different thresholds, we conclude that a Z_H threshold of 10 dBZ provides the best balance between sensitivity and noise.

The z_e for each column is nominally the highest level with a reflectivity greater than or equal to 10 dBZ. In order to ensure that individual echo top altitudes are associated with deep convection, we require the GridRad altitude bin closest to the ERA-I tropopause in each column to contain $Z_H \geq 20$ dBZ. This eliminates many scans in which the vertical profile of Z_H is discontinuous or the convective anvil echo top altitude lies above the tropopause over broad regions. One thing to note is that it is possible, by implementing this criteria, that we are not capturing every tropopause-overshooting event. To further reduce the number of false echo top identifications in situations with unrealistic reflectivity profiles, we also require that the two altitude levels immediately below a potential echo top also contain valid Z_H measurements. If this condition is not met, the column is searched for the next highest Z_H value exceeding 10 dBZ and the process is repeated until a measurement satisfying the criteria is found or the bottom of the column is reached.

To evaluate the accuracy of echo top altitudes derived from the GridRad data, we compare $Z_H = 10$ dBZ echo top altitudes detected from GridRad with high-resolution, spaceborne 10 dBZ echo top altitudes detected by the CloudSat Cloud Profiling Radar (CPR) in Figure 2. CloudSat is a Sun-synchronous low Earth-orbiting satellite that is part of the National Aeronautics and Space Administration (NASA) "Afternoon" constellation of satellites (the A-Train). CloudSat has nominal equator-crossing times of 0130 and 1330 local time. The CloudSat CPR is a nadir-pointing, 94 GHz (3 mm wavelength) cloud radar that observes Z_H from −28 to ~20 dBZ (Stephens et al., 2002). The along-track resolution of the CPR is 1.7 km and the vertical resolution is 480 m,

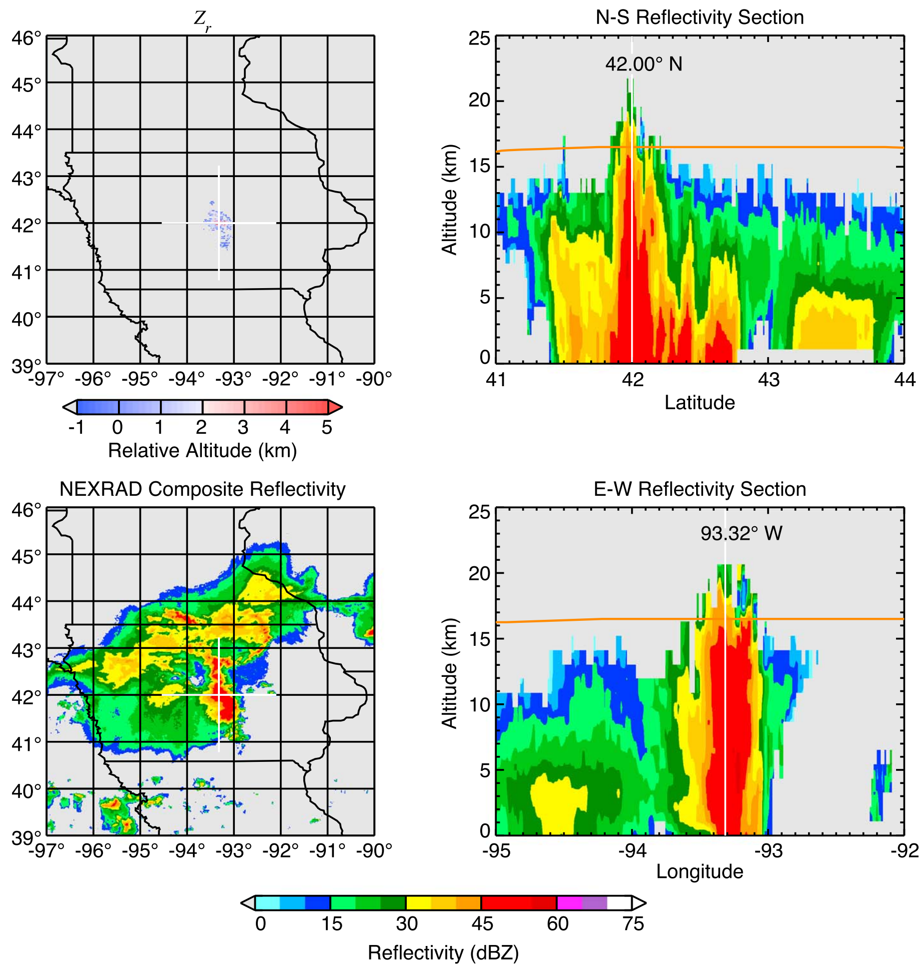

Figure 3. Example of a four-panel image used to quality control the +1 km overshoot identifications. This example is from 11 July 2011 at 0900Z. The orange line on the vertical cross-section plots indicates the primary tropopause. The white crosshairs on the maps mark the center of one overshoot and show the alignment of the cross sections. The vertical white lines on the cross sections mark the center of the overshooting region of the overshoot being evaluated.

with Z_H profiles oversampled at 1.1 km along track and 240 m in the vertical. CloudSat was placed into orbit in April 2006 and has been transmitting data since. Prior to 17 April 2011, observations were made continuously both day and night, but a battery failure on that date reduced operating capabilities to daytime-only observations and caused CloudSat to lose formation with the A-Train. CloudSat reentered the A-Train formation on 15 May 2012. In order to enable comparisons with the CloudSat CPR, a special set of GridRad analyses were created along CloudSat orbits over the contiguous United States for the years 2006 to 2016. Figure 2 shows a frequency distribution of the resulting differences in the 10 dBZ echo top altitudes for more than 200,000 coincident profiles. This comparison demonstrates that GridRad echo top altitudes are consistent with those observed from higher-resolution platforms, with nearly unbiased mean differences between GridRad and the CloudSat CPR and an uncertainty (standard deviation) of approximately ±1 km. Additional evaluation of this comparison demonstrates that mean absolute differences range from 0.5 to 1 km across the GridRad domain, with larger differences more common in locations with sparser radar coverage (not shown).

Overshooting convection is defined as echoes located above the tropopause. The echo top height relative to the tropopause, $z_r = z_e - z_{\mathrm{trop}}$, is computed from the NEXRAD echo top altitudes and the simultaneous ERA-I tropopause altitudes. To provide a more convenient framework for the following analysis, contiguous regions of overshooting columns (grid boxes) are grouped into what we refer to as overshooting events or "overshoots." Grid boxes are considered to be contiguous if they touch either along their edges or at a corner.

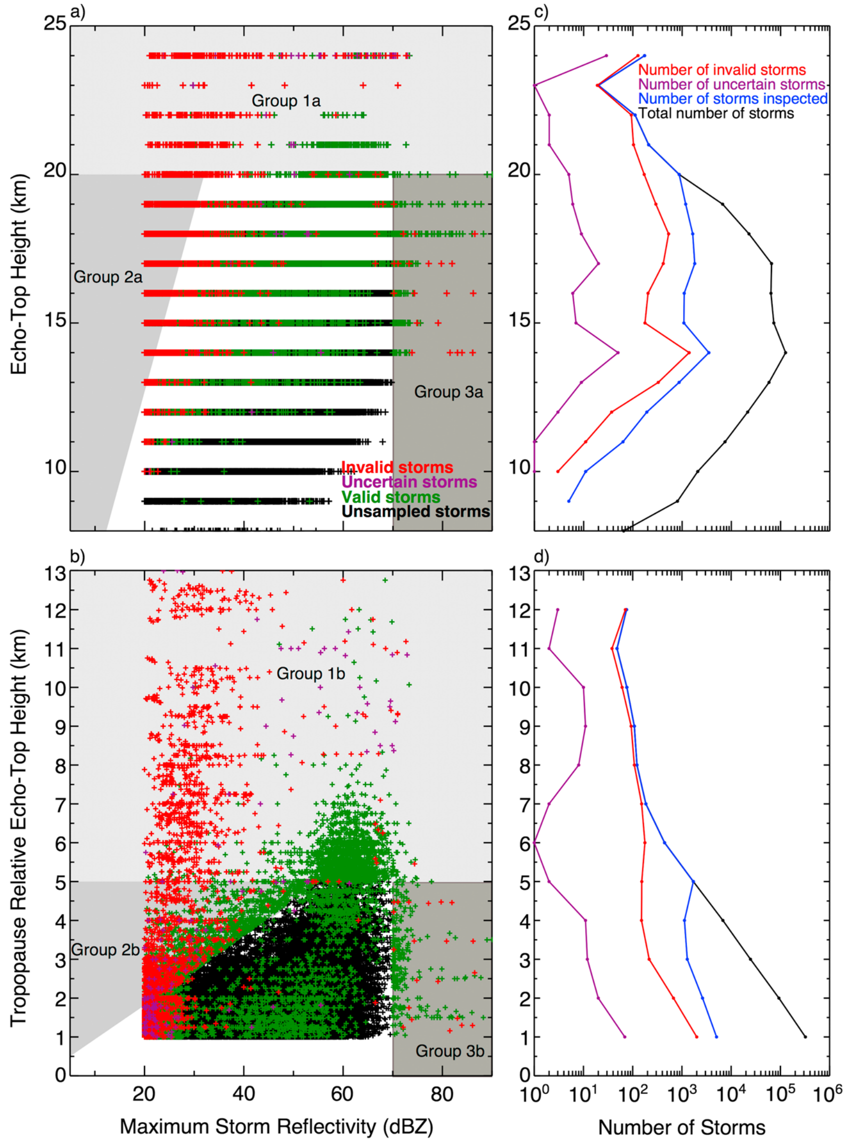

Figure 4. (a) Scatterplot of maximum echo top height z_e in each overshoot as a function of maximum reflectivity in the overshoot. (b) Same as Figure 4a but for z_r. (c) Number of echo tops as a function of altitude (black); number of overshoots inspected at each level (blue); number of invalid and uncertain overshoots at each level (red and purple, respectively). (d) Same as Figure 4c but for z_r.

Table 1
Classification of +1 km Overshoots Reviewed for Each Group

Group	Description	Number of overshoots	Valid %	Invalid %	Uncertain %
Group 1a	$z_e \geq 20$ km	1,386	60.2	36.9	2.8
Group 2a	$z_e < 20$ km, high z_e, low R	5,754	49.5	49.1	1.4
Group 3a	$z_e < 20$ km, $R \geq 70$ dBZ	294	92.2	7.8	0.0
Group 1b	$z_r \geq 5$ km	2,769	67.6	31.0	1.4
Group 2b	$z_r < 5$ km, high z_r, low R	4,348	68.4	30.5	1.0
Group 3b	$z_r < 5$ km, $R \geq 70$ dBZ	277	92.1	7.9	0.0
Group 4	Complementary subsample	1,000	97.8	1.7	0.5

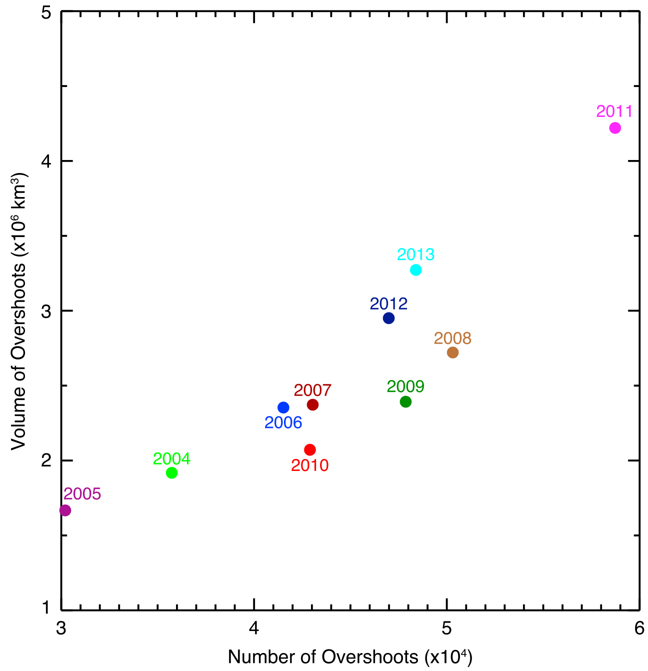

Figure 5. Total overshooting volume as a function of the number of +1 km overshoots during each year (MAMJJA only). The color codes are the same for all figures with data stratified by year.

There are uncertainties in both the altitudes of the echo tops and the height of the tropopause. In order to analyze overshooting events that we are confident actually penetrate into the stratosphere, in the remainder of the paper we restrict our analysis to overshoots that have $z_r \geq 1$ km. These are referred to as +1 km overshoots. During the study period we identify 449,745 such overshoots.

3.3. Quality Control

A sample of the +1 km overshoots is subjectively evaluated to validate the echo top identification scheme. Overshoots are evaluated by visually inspecting composite reflectivity maps, tropopause-relative altitude maps, and vertical reflectivity cross sections through the highest echo top of each sampled overshoot event. Each inspected overshoot is subjectively assigned to one of three categories: valid, invalid, or uncertain. Figure 3 provides an example of one of the larger valid overshooting events. This classification is based on the strong and continuous vertical reflectivity structure and the realistic reflectivity map. We reviewed radiosonde vertical temperature profile plots from nearby sites at 1200 UTC and found the estimate of the tropopause to be very accurate. Overshooting events that are obviously unphysical in appearance are deemed invalid. Examples of unphysical echoes include the following: narrow rays of echoes extending from the radar to the stratosphere surrounded by clear air; rings of uniform reflectivity surrounding the radar site; echoes in the stratosphere but none in the troposphere below to indicate the presence of deep convection. Overshoots classified as uncertain cannot be definitively identified as either valid or invalid based on their appearance. They typically have narrow vertical columns of reflectivity and are often associated with very weak echoes in the troposphere. As will be seen below, the number of these overshoots is small. Overshoots deemed invalid or uncertain are removed from further analysis.

To create a targeted sampling scheme for the +1 km overshoots, the sample population is partitioned into seven groups based on the maximum echo top altitude (either z_e or z_r) and the maximum Z_{H} observed in the overshoot, which is typically in the troposphere. The goal is to subjectively evaluate all of the very deep (extreme) overshoots, a large fraction of the events with high echo tops and low tropospheric Z_{H} (which may be questionable), and a representative sample of the overshoots with high tropospheric Z_{H} (which we believe a priori to be realistic). The partitioning is illustrated in Figure 4. The seven groups are as follows:

- 1a: Deep overshoots with $z_e \geq 20$ km (light gray region in Figure 4a)
- 1b: Deep overshoots with $z_r \geq 5$ km (light gray region in Figure 4b)
- 2a: Overshoots with relatively high z_e, $z_e < 20$ km, and low maximum Z_{H} (medium gray region in Figure 4a)
- 2b: Overshoots with relatively high z_r, $z_r < 5$ km, and low maximum Z_{H} (medium gray region in Figure 4b)
- 3a: Overshoots with $z_e < 20$ km and $Z_{\mathrm{H}} \geq 70$ dBZ (dark gray region in Figure 4a)
- 3b: Overshoots with $z_r < 5$ km and $Z_{\mathrm{H}} \geq 70$ dBZ (dark gray region in Figure 4b)
- 4: Overshoots that are not in groups 1a, 1b, 2a, 2b, 3a, or 3b

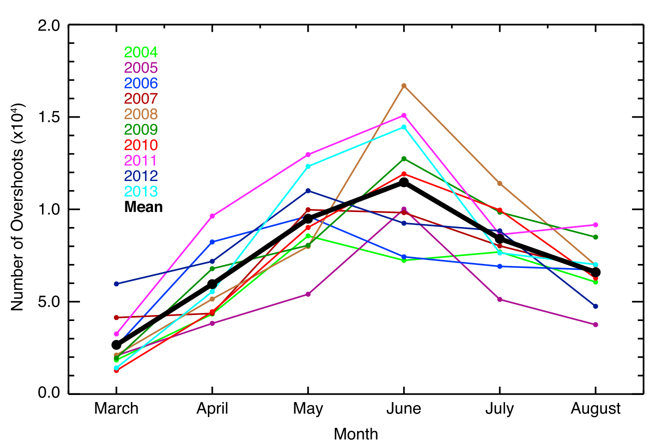

Figure 6. Number of +1 km overshoots per month for each year. Each color on the plot corresponds to a given year shown in the key. The bold black line shows the average for each month.

The number of overshoots evaluated in each group is provided in Table 1, which summarizes the results of the subjective quality control process. Every overshoot in groups 1a, 2a, 3a, 1b, 2b, and 3b is inspected. A random sample of 1,000 overshoots from group 4 is analyzed. In all, a total of 12,848 overshoots are reviewed for quality control. Because some overshoots fall into more than one category (groups in Figure 4a can overlap with groups in Figure 4b), this number is less than the total of the overshoots in each group shown in Table 1. The overshoots in group 4,

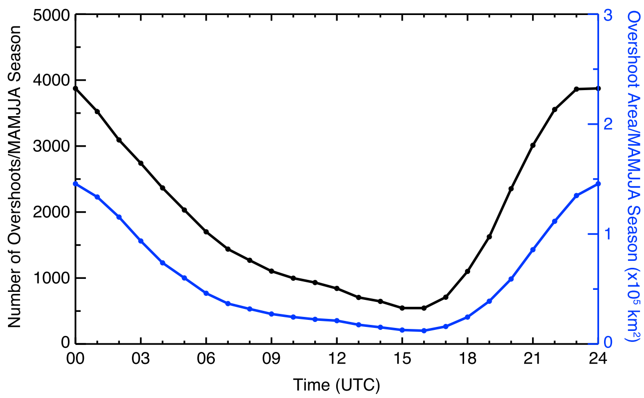

Figure 7. Climatological average number of overshoots (black) and climatological average total overshoot area (blue) during MAMJJA at each analysis time.

however, do not overlap with any of the other groups and are used to estimate the number of invalid/uncertain overshoots remaining in the analysis.

Note that the order in which the symbols are plotted in Figure 4 (symbols for invalid overshoots plotted on top of symbols for valid overshoots) gives the impression that there are more invalid than valid overshoots. This is not the case, however, as can be seen in Table 1. Note that the majority of the overshoots, even in groups 1a and 1b (~60% and ~68%, respectively), are classified as valid. In group 1a, the valid overshoots are primarily those with z_e of 20 or 21 km and maximum storm overshoot $Z_H > 50$ dBZ. In group 1b, the valid overshoots are primarily those with z_r between 5 and 7 km and maximum $Z_H > 50$ dBZ. In both groups a very small number of the deepest overshoots have realistic Z_H profiles. About half the overshoots in groups 2a and 2b (~49.5% and ~68.4%, respectively), which have high tops and low Z_H, are found to be valid. A large majority of the inspected overshoots in group 4 are valid, with about 2.2% identified as invalid or uncertain.

Figures 4c and 4d show the number of overshoots, the number of overshoots inspected, and the status of the inspected overshoots at each altitude level in terms of z_e and z_r, respectively. Note that the abscissae in these plots are logarithmic. In general, the fraction of invalid or uncertain overshoots increases with height above the tropopause.

All of the overshoots classified as uncertain or invalid are removed from the following statistical analysis. After eliminating these cases, 445,694 +1 km overshoots remain. Based on the number of invalid and uncertain overshoots identified in the sample from group 4, we estimate that only approximately 9,612 of the overshoots (<3%) included in the analysis are invalid or uncertain. These overshoots do not significantly affect the results. Based on the exhaustive subjective analysis of groups 1–3, we believe that all of the very high overshoots included in the analysis population are valid.

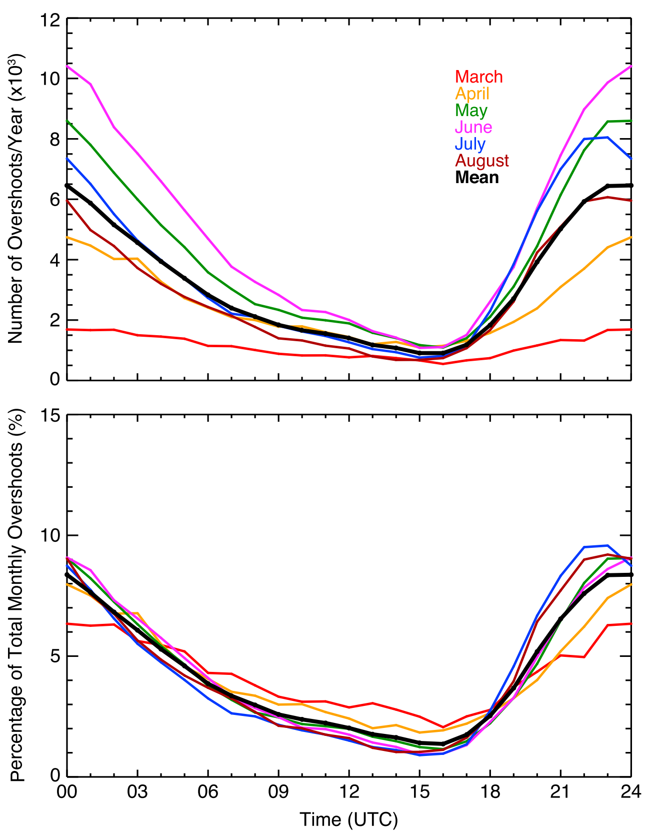

Figure 8. (top) Number of overshooting events per year at each hour stratified by month. (bottom) Percentage of overshooting events at each hour stratified by month. The black lines are the 10 year climatological means.

4. Results

4.1. Overview

The following analysis includes all overshooting events that extend at least 1 km above the ERA-I tropopause, which excludes a large number of shallow overshooting events that penetrate less than 1 km into the stratosphere. Because individual overshooting events may have lifetimes as short as 5 to 10 min, some overshoots are missed by the hourly sampling. Likewise, overshoots may last up to several hours causing them to be counted more than once. Thus, due to the temporal resolution the total number of actual overshooting events may be different than the numbers presented here. The issue of overshoot lifetime and sampling will be addressed in future research by conducting reflectivity analyses with a higher temporal resolution.

Each MAMJJA period contains 184 days, so this 10 year study comprises a total of $24 \times 184 \times 10 = 44,160$ instantaneous hourly analyses. A total of 445,694 +1 km overshoots occur during this period, which corresponds to approximately 44,569 +1 km overshoots per year or 242 per day, on average.

4.2. Interannual, Monthly, and Diurnal Variations

Figure 5 shows the relationship between the total number of +1 km overshoots for each year and the total overshooting volume of those years. Overshoot volume is the product of the tropopause-relative height of each column in the overshoot and the associated grid box area, summed over the overshoot. The number of overshooting events varies by a factor of ~2 during the study period while the total overshoot volume varies by a

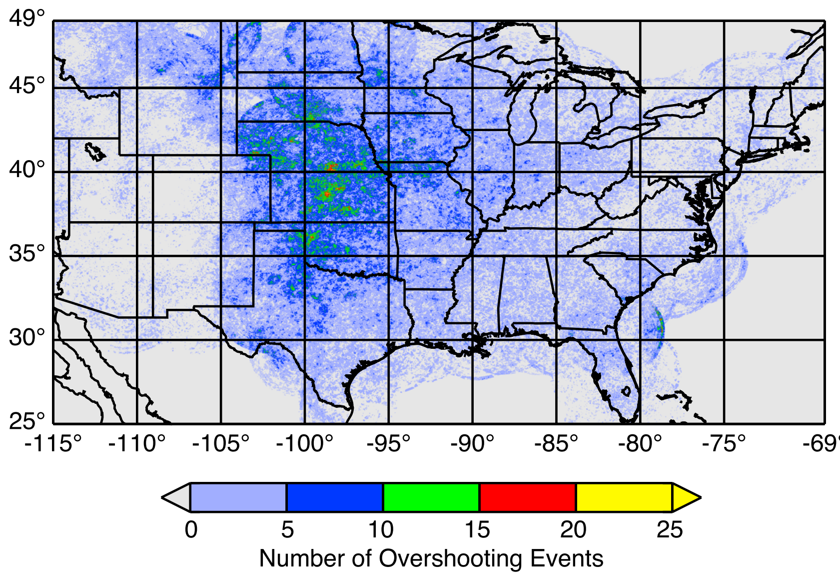

Figure 9. Number of instances during the study period that overshooting convection reached at least 1 km above the tropopause in each grid box.

factor of ~2.5. The approximately linear relationship between the two quantities indicates that there is little interannual variation in the size distribution of the overshoots, and the total overshoot volume is controlled primarily by the number of overshooting events for that year. The change from legacy resolution to superresolution does not appear to have had a significant effect on overshoot detection. Years with superresolution data include some of the lowest (2010) and highest (2009, 2011, and 2013) years in terms of overshoot occurrence, which suggests that the variations are real and not due to changes in the NEXRAD data.

Figure 6 shows the monthly overshoot occurrence for each year of the study period. On average May, June, and July have more overshoots than March, April, and August, with June having approximately 2 times as many as April. The largest number of overshooting events for any month is observed in June 2008, while the fewest are seen in March 2010.

The diurnal cycles of overshooting occurrences and overshoot area for the 10 year average are plotted in Figure 7. A large diurnal cycle exists, with a peak that occurs from 22 to 02 UTC (late afternoon to early evening local time). The minimum number of events and overshoot area occur between 13 and 17 UTC (late morning to early afternoon local time). The diurnal cycle of overshooting convection is consistent with the known diurnal cycle of summertime precipitation (e.g., Dai et al., 1999). The similarity of the two curves implies that the diurnal variation in overshoot area is primarily a result of variations in the number of overshoots, not variations in their overshoot sizes.

Figure 8 top shows the variation of the diurnal cycle by month over the warm season (MAMJJA). If the curves are normalized by the number of overshoots in that month (Figure 8, bottom), the shapes of the curves are nearly identical, with the exception of March, which has a very weak diurnal cycle. This demonstrates that the amplitude of the diurnal cycle is proportional to the total number of overshoots per month. There may be small systematic variations in the shape of the diurnal cycle near the diurnal peak, but this could also be due to the limited sample size of this study.

4.3. Geographic Distribution of Overshooting Events

The geographic distribution of overshooting event occurrences is shown in Figure 9. Minor artifacts from the gridding process are visible as circular features centered on individual radars. These artifacts arise from several factors, including the lack of scans at high-elevation angles, which results in an absence of observations at high altitudes close to the radar locations, and limited overlap from adjacent radars. This is most common in the western part of the domain and along the edges of the NEXRAD network area.

The vast majority of overshooting events occur over the central plains, with few occurrences over the Appalachian Mountains or in the southeast. There is evidence of a weak secondary maximum along the East

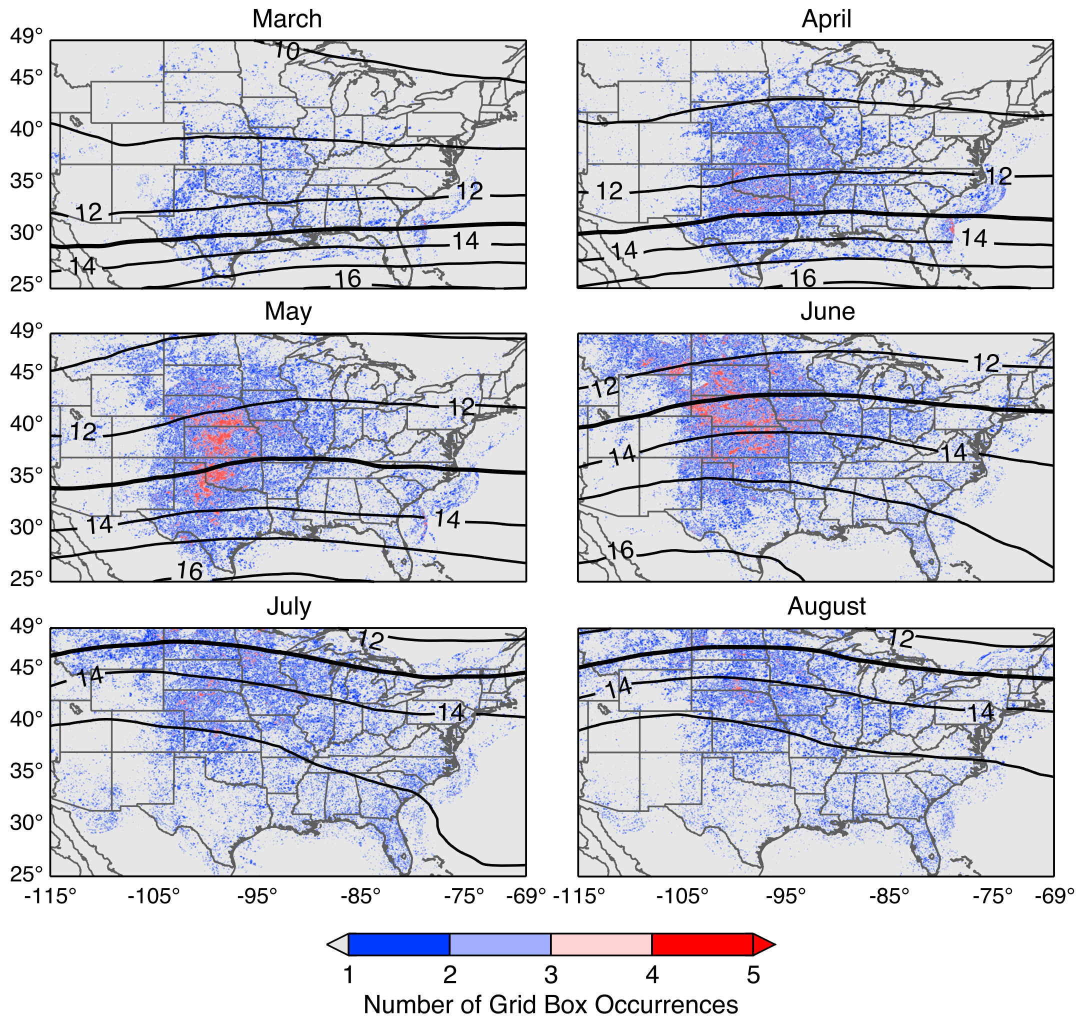

Figure 10. Monthly maps of the number of overshooting events in each grid box (shading) and climatological tropopause height in km (black contours). For easier comparison, the 13 km contour level is drawn with a heavy line. The maximum number of overshoot events over any grid box is 15 and occurs in May.

Coast extending from northern Florida to North Carolina. Because the radar network coverage east of the Mississippi River is generally very good, we conclude that the lack of overshooting events in the eastern part of the domain is real and not a result of data issues.

The occurrence of overshooting convection is closely connected to the seasonal evolution of the tropopause altitude, as can be seen in Figure 10, which shows the number of overshoots within each grid box for each month along with the climatological monthly mean tropopause height. The altitude of the tropopause generally increases as the year progresses at all locations in the study area. As the tropopause rises, overshooting shifts northward along with the region of lower tropopause altitudes. The exception is in the southeast, where overshooting is more common in June, July, and August than earlier in the year. In all months, few +1 km overshoots are observed in locations with an average tropopause height $\gtrsim$15.5 km.

4.4. Vertical Distribution

The frequency distribution of the maximum echo top altitude in each overshoot for the entire domain is shown in Figure 11 for each month. The total distribution for all six months is shown in black. The peak occurrences in the overshooting echo top height for March, April, May, and June is 14 km. In July and August, the peaks shift upward to 17 km. The cumulative fraction for all months, integrated from the top down, is plotted in gray. The results show that only ~5% of +1 km overshoots have tops that reach 18 km or higher, but ~50% of the overshoots have tops reaching at least 15 km.

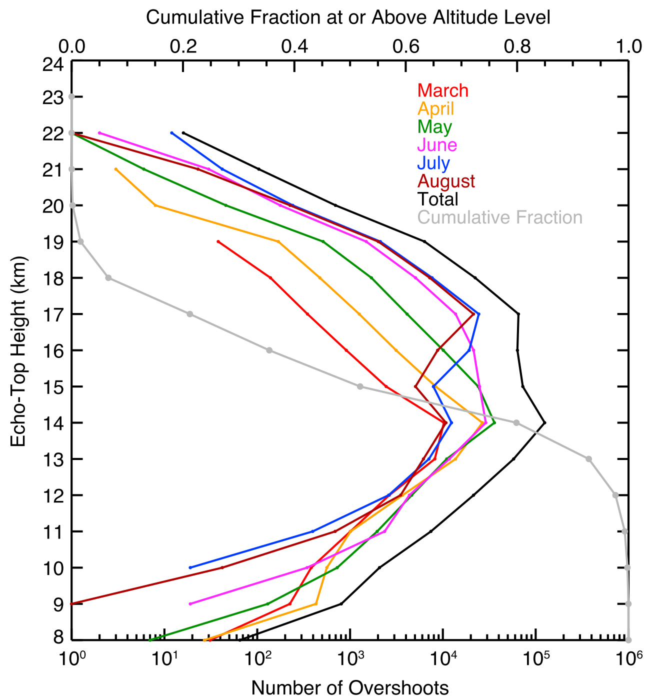

Figure 11. Histograms of the maximum echo top height, z_e, in each overshooting event by month (colors). The vertical bin size is 1 km. The histogram for the entire study period is drawn in black. Note the logarithmic scale. The cumulative histogram (gray), expressed as the fraction of all the +1 km overshoots and plotted on a linear scale, is computed by summing from the top down.

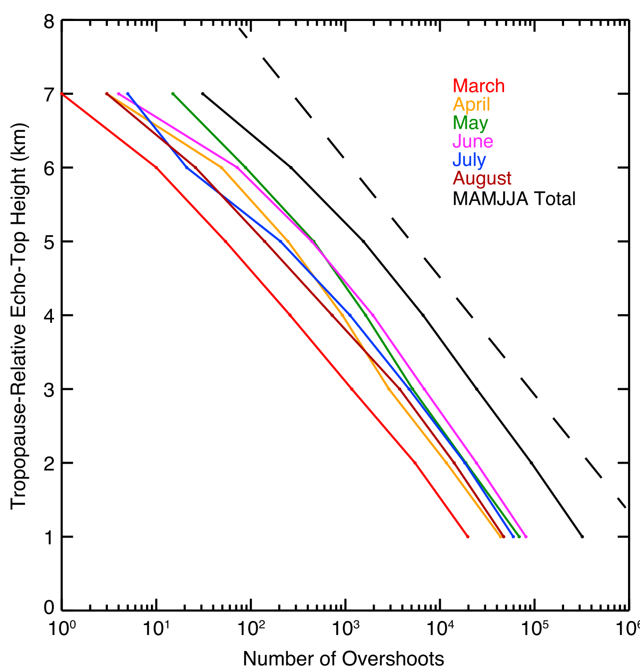

Figure 12. Histograms of the maximum tropopause-relative echo top height, z_r, in each overshooting event by month. Bin sizes are 1 km. The tropopause-relative echo top height histogram for the entire study period is drawn in black. The dashed line, which is drawn for reference, is an exponential function with a scale height of ~1.0 km.

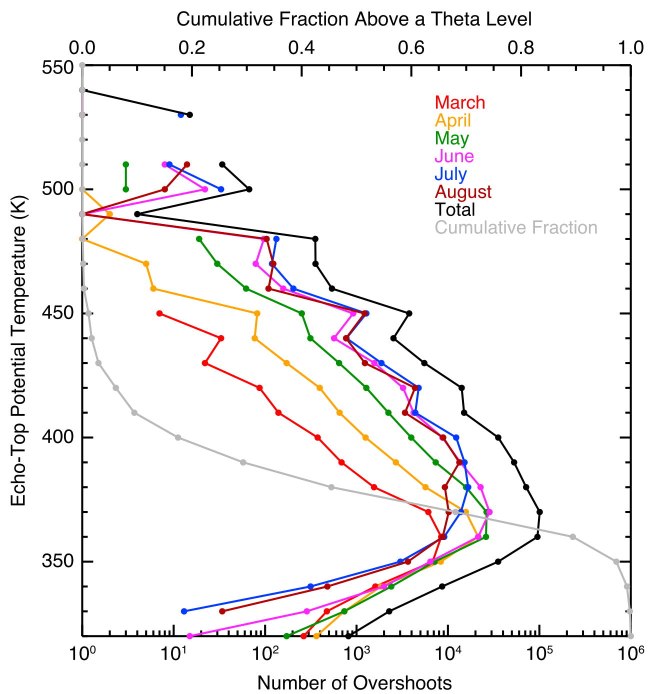

Figure 13. Histograms of the maximum echo top potential temperature in each overshooting event by month (colors). Bin sizes are 10 K. The histogram for the entire study period is drawn in black. The cumulative histogram (gray), expressed as the fraction of all the +1 km overshoots and plotted on a linear scale, is computed by summing from the top down.

The number of overshoots that reach a given altitude relative to the tropopause falls off approximately exponentially with altitude, as can be seen in Figure 12, with a very small fraction of the overshooting events reaching 6 or 7 km above the tropopause. The total number of overshooting events varies by month (see Figure 6), but the vertical distribution is similar in all months. The scale height for the number of overshoots is ~1 km for the first few kilometers above the tropopause. Above that the frequency decreases more rapidly. May is observed to have consistently more overshoots at higher tropopause-relative altitudes than July, which is consistent with results observed in Bigelbach et al. (2014).

Histograms of the number of overshoots reaching various potential temperature levels are shown in Figure 13. The peak altitude is 360 K in March, April, and May and between 370 and 390 K in June, July, and August. The highest echo top potential temperatures observed are near 600 K. Approximately 45% of the +1 km overshoots have echo tops with potential temperature values that are 380 K or higher, which places them in the stratospheric overworld.

The geographic distribution of the maximum echo top potential temperature in each grid box for the climatology is shown in Figure 14. The deepest overshoots occur in the Central Plains. Relatively few occurrences of echo tops above the 460 K level are seen, but tops above 400 K are common.

5. Conclusions

This study merges WSR-88D radar observations from the NEXRAD network into hourly, high-resolution, three-dimensional, gridded reflectivity analyses for a large part of the contiguous United States. The reflectivity data are combined with tropopause height estimates from the ERA-Interim reanalysis to create a 10 year data set of tropopause-overshooting convective events for the March–August period. Using improved quality control and data processing procedures, as well as a much longer record, this study expands upon the results in Solomon et al. (2016) and includes an analysis of the interannual variability of overshooting convection over the study area. Neighboring atmospheric columns that overshoot the ERA-I

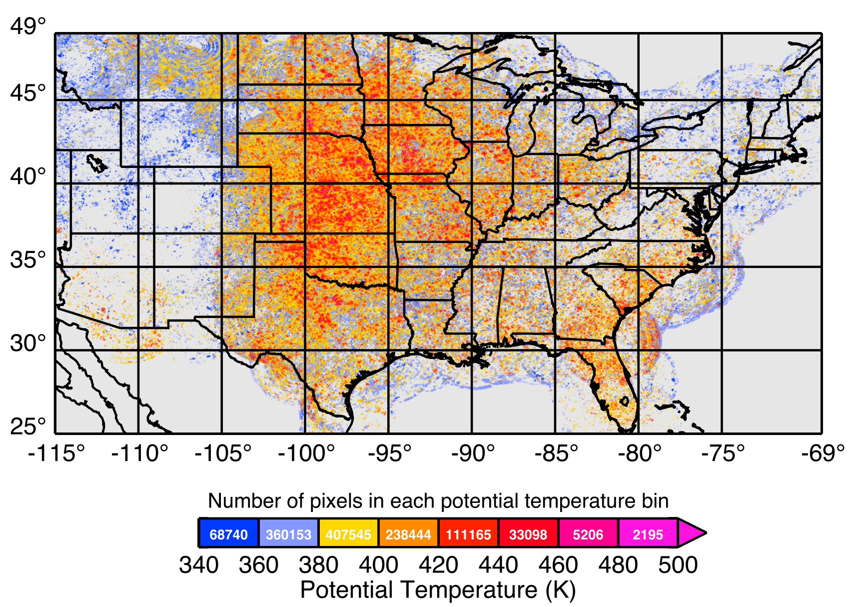

Figure 14. Maximum observed echo top potential temperature for each grid box. The numbers inside the color bar are the number of grid boxes with maximum potential temperatures in that range.

tropopause by 1 km or more are combined into what we refer to as +1 km overshoots. After applying the quality control procedures, the number of +1 km overshoots used in the statistical analysis is 445,694.

During the study period, the total yearly volume of overshooting events in the stratosphere varies by about a factor of 2.5. This could lead to interannual variations in the moistening of the lower stratosphere by deep convection. Most of this change is due to variations in the number of overshoots that occur each year. Within the MAMJJA analysis period, the highest number of overshooting events are found in May, June, and July; fewer overshoots occur in March, April, and August.

Overshooting events are most likely to occur over the central United States between 22 and 02 UTC (late afternoon to early evening local time). This late afternoon-early evening maximum is consistent with the known diurnal cycle of warm season continental precipitation.

Although about half the overshoots reach altitudes of 15 km or higher, the number of overshooting events decreases exponentially with height above the tropopause; and it is rare to observe echoes 6 km or more above the tropopause (∼321 overshoot events in 10 years). The highest echo tops observed in this study reached an altitude of 24 km. High echo tops are more likely in July and August than in March, April, May, or June, but the tropopause is also higher later in the summer. The net result is that more overshoots penetrate deep into the stratosphere in May and June.

Approximately half of the analyzed overshoots have tops at or above the 380 K level, which shows that extratropical overshooting convection frequently extends into the stratospheric overworld. These overshooting events are a likely source for the enhanced water vapor observed in the quasi-stationary North American monsoon anticyclone (Alcala & Dessler, 2002; Dessler & Sherwood, 2004; Hanisco et al., 2007) and could potentially affect stratospheric chemistry (Anderson et al., 2012, 2017). The physical mechanisms responsible for the observed geographic distribution of overshooting events are not clear and will be the subject of future study. Further research is underway to understand the differences in overshooting occurrence found in the satellite analysis of Bedka et al. (2010) and in the NEXRAD analysis presented here and in Solomon et al. (2016).

Acknowledgments
Funding for this work was provided by the National Science Foundation through grants AGS-1522906 and AGS-1522910 to Texas A&M University and the University of Oklahoma, respectively. Radar data were downloaded from the NOAA National Centers for Environmental Information (http://www.ncdc.noaa.gov). The NEXRAD data files were translated to netCDF format using the NOAA Weather and Climate Toolkit (https://www.ncdc.noaa.gov/wct/). ECMWF ERA-Interim reanalysis data were downloaded from the National Center for Atmospheric Research Research Data Archive (NCAR RDA; http://rda.ucar.edu/datasets/ds627.0/). GridRad data are available at the NCAR RDA (http://rda.ucar.edu/datasets/ds841.0/).

References

Alcala, C. M., & Dessler, A. E. (2002). Observations of deep convection in the tropics using the Tropical Rainfall Measuring Mission (TRMM) precipitation radar. *Journal of Geophysical Research*, *107*(D24), 4792. https://doi.org/10.1029/2002JD002457

Anderson, J. G., Weisenstein, D. K., Bowman, K. P., Homeyer, C. R., Smith, J. B., Wilmouth, D. M., … Wofsy, S. C. (2017). Stratospheric ozone over the United States in summer linked to observations of convection and temperature via chlorine and bromine catalysis. *Proceedings of the National Academy of Sciences of the United States of America*, *114*, E4905–E4913. https://doi.org/10.1073/pnas.1619318114

Anderson, J. G., Wilmouth, D. M., Smith, J. B., & Sayres, D. S. (2012). UV dosage levels in summer: Increased risk of ozone loss from convectively injected water vapor. *Science*, *337*, 835–839. https://doi.org/10.1126/science.1222978

Bedka, K., Brunner, J., Dworak, R., Feltz, W., Otkin, J., & Greenwald, T. (2010). Objective satellite-based detection of overshooting tops using infrared window channel brightness temperature gradients. *Journal of Applied Meteorology and Climatology*, *49*, 181–202. https://doi.org/10.1175/2009JAMC2286.1

Berendes, T. A., Mecikalski, J. R., MacKenzie Jr., W. M., Bedka, K. M., & Nair, U. S. (2008). Convective cloud identification and classification in daytime satellite imagery using standard deviation limited adaptive clustering. *Journal of Geophysical Research*, *113*, D20207. https://doi.org/10.1029/2008JD010287

Bigelbach, B. C., Mullendore, G. L., & Starzec, M. (2014). Differences in deep convective transport characteristics between quasi-isolated strong convection and mesoscale convective systems using seasonal WRF simulations. *Journal of Geophysical Research: Atmospheres*, *119*, 11,445–11,455. https://doi.org/10.1002/2014JD021875

Bowman, K. P., & Homeyer, C. R. (2017). GridRad—Three-dimensional gridded NEXRAD WSR-88D radar data. Retrieved from http://rda.ucar.edu/datasets/ds841.0/

Chagnon, J. M., & Gray, S. L. (2010). A comparison of stratosphere-troposphere transport in convection-permitting and convection-parameterizing simulations of three mesoscale convective systems. *Journal of Geophysical Research*, *115*, D24318. https://doi.org/10.1029/2010JD014421

Crum, T. D., & Alberty, R. L. (1993). The WSR-88D and the WSR-88D operational support facility. *Bulletin of the American Meteorological Society*, *74*(9), 1669–1687.

Dai, A., Giorgi, F., & Trenberth, K. E. (1999). Observed and model-simulated diurnal cycles of precipitation over the contiguous United States. *Journal of Geophysical Research*, *104*(D6), 6577–6402.

Dee, D. P., Uppala, S. M., Simmons, A. J., Berrisford, P., Poli, P., Kobayashi, S., … Vitart, F. (2011). The ERA-Interim reanalysis: Configuration and performance of the data assimilation system. *Quarterly Journal of the Royal Meteorological Society*, *137*(656), 553–597. https://doi.org/10.1002/qj.828

Dessler, A. E., & Sherwood, S. C. (2004). Effect of convection on the summertime extratropical lower stratosphere. *Journal of Geophysical Research*, *109*, D23301. https://doi.org/10.1029/2004JD005209

Gettelman, A., Hoor, P., Pan, L. L., Randel, W. J., Hegglin, M. I., & Birner, T. (2011). The extratropical upper troposphere and lower stratosphere. *Reviews of Geophysics*, *49*, RG3003. https://doi.org/10.1029/2011RG000355

Gray, S. L. (2003). A case study of stratosphere to troposphere transport: The role of convective transport and the sensitivity to model resolution. *Journal of Geophysical Research*, *108*(D18), 4590. https://doi.org/10.1029/2002JD003317

Hanisco, T. F., Moyer, E. J., Weinstock, E. M., Clair, J. M. S., Sayres, D. S., Smith, J. B., … Bui, T. P. (2007). Observations of deep convective influence on stratospheric water vapor and its isotropic composition. *Geophysical Research Letters*, *34*, L04814. https://doi.org/10.1029/2006GL027899

Holton, J. R., Haynes, P. H., McIntyre, M. E., Douglass, A. R., Rood, R. B., & Pfister, L. (1995). Stratosphere-troposphere exchange. *Reviews of Geophysics*, *33*, 403–439. https://doi.org/10.1029/95RG02097

Homeyer, C. R. (2014). Formation of the enhanced-V infrared cloud top feature from high-resolution three-dimensional radar observations. *Journal of the Atmospheric Sciences*, *71*, 332–348. https://doi.org/10.1175/JAS-D-13-079.1

Homeyer, C. R., & Bowman, K. P. (2017). Algorithm description document for version 3.1 of the three-dimensional gridded NEXRAD WSR-88D radar (GridRad) dataset (Tech. Rep.). GridRad.org. https://doi.org/gridrad.org/pdf/GridRad-v3.1-Algorithm-Description.pdf

Homeyer, C. R., & Kumjian, M. R. (2015). Microphysical characteristics of overshooting convection from polarimetric radar observations. *Journal of the Atmospheric Sciences*, *72*, 870–891. https://doi.org/10.1175/JAS-D-13-0388.1

Homeyer, C. R., Pan, L. L., & Barth, M. C. (2014). Transport from convective overshooting of the extratropical tropopause and the role of large-scale lower stratosphere stability. *Journal of Geophysical Research: Atmospheres*, *119*, 2220–2240. https://doi.org/10.1002/2013JD020931

Homeyer, C. R., Pan, L. L., Dorsi, S. W., Avallone, L. M., Weinheimer, A. J., O'Brien, A. S., … Campos, T. L. (2014). Convective transport of water vapor into the lower stratosphere observed during double-tropopause events. *Journal of Geophysical Research: Atmospheres*, *119*, 10,941–10,958. https://doi.org/10.1002/2014JD021485

Homeyer, C. R., McAuliffe, J. D., & Bedka, K. M. (2017). On the development of above-anvil cirrus plumes in extratropical convection. *Journal of the Atmospheric Sciences*, *74*, 1617–1633. https://doi.org/10.1175/JAS-D-16-0269.1

Lakshmanan, V., Smith, T., Hondl, K., Stumpf, G. J., & Witt, A. (2006). A real-time, three-dimensional, rapidly updating, heterogeneous radar merger technique for reflectivity, velocity, and derived products. *Weather and Forecasting*, *22*, 802–823.

Langston, C., Zhang, J., & Howard, K. (2007). Four-dimensional dynamic radar mosaic. *Journal of Atmospheric and Oceanic Technology*, *24*, 776–790. https://doi.org/10.1175/JTECH2001.1

Lindsey, D. T., & Grasso, L. (2008). An effective radius retrieval for thick ice clouds using GOES. *Journal of Applied Meteorology and Climatology*, *47*, 1222–1231.

Liu, N., & Liu, C. (2016). Global distribution of deep convection reaching tropopause in 1 year GPM observations. *Journal of Geophysical Research: Atmospheres*, *121*, 3824–3842. https://doi.org/10.1002/2015JD024430

Rosenfeld, D., Woodley, W. L., Lerner, A., Kelman, G., & Lindsey, D. T. (2008). Satellite detection of severe convective storms by their retrieved vertical profiles of cloud particle effective radius and thermodynamic phase. *Journal of Geophysical Research*, *113*, D04208. https://doi.org/10.1029/2007JD008600

Ruzanski, E., & Chandrasekar, V. (2012). An investigation of the short-term predictability of precipitation using high-resolution composite radar observations. *Journal of Applied Meteorology and Climatology*, *51*, 912–925. https://doi.org/10.1175/JAMC-D-11-069.1

Solomon, D. L., Bowman, K. P., & Homeyer, C. R. (2016). Tropopause-penetrating convection from three-dimensional gridded NEXRAD data. *Journal of Applied Meteorology and Climatology*, *55*, 465–478. https://doi.org/10.1175/JAMC-D-15-0190.1

Stephens, G. L., Vane, D. G., Boain, R. J., Mace, G. G., Sassen, K., Wang, Z., … CloudSat Science Team (2002). The CloudSat mission and the A-train. a new dimension of space-based observations of clouds and precipitation. *Bulletin of the American Meteorological Society*, *83*, 1771–1790. https://doi.org/10.1175/BAMS-83-12-1771

Stohl, A., Wernli, H., James, P., Bourqui, M., Forster, C., Liniger, M. A., … Sprenger, M. (2003). A new perspective of stratosphere-troposphere exchange. *Bulletin of the American Meteorological Society*, *84*, 1565–1573. https://doi.org/10.1175/BAMS-84-11-1565

Wang, P. K. (2003). Moisture plumes above thunderstorm anvils and their contributions to cross-tropopause transport of water vapor in midlatitudes. *Journal of Geophysical Research*, *108*, 4194. https://doi.org/10.1029/2002JD002581

Wang, P. K. (2007). The thermodynamic structure atop a penetrating convective thunderstorm. *Atmospheric Research*, *83*, 254–262.

WMO (1957). Meteorology—A three-dimensional science: Second session of the commision for aerology. *WMO Bulletin*, *IV*(4), 134–138.

Zhang, J., Wang, S., & Clarke, B. (2004). WSR-88D reflectivity quality control using horizontal and vertical reflectivity structure. *Proceedings of llth Conference on Aviation, Range and Aerospace Meteorology*, *1*, 5–6.

Zhang, J., Howard, K., & Gourley, J. J. (2005). Constructing three-dimensional multiple-radar reflectivity mosaics: Examples of convective storms and stratiform rain echoes. *Journal of Atmospheric and Oceanic Technology*, *22*, 30–42.

Zhang, J., Howard, K., Langston, C., Vasiloff, S., Kaney, B., Arthur, A., … Dempsey, C. (2011). National mosaic and multi-sensor QPE (NMQ) system: Description, results, and future plans. *Bulletin of the American Meteorological Society*, *92*, 1321–1338. https://doi.org/10.1175/2011BAMS-D-11-00047.1